

# US Backscatter for Liver Fat Quantification: An AIUM-RSNA QIBA Pulse-Echo Quantitative Ultrasound Initiative

Keith A. Wear, PhD • Aiguo Han, PhD • Jonathan M. Rubin, MD, PhD • Jing Gao, MD • Roberto Lavarello, PhD • Guy Cloutier, PhD • Jeffrey Bamber, PhD • Theresa Tutill, PhD

From the Center for Devices and Radiological Health, U.S. Food and Drug Administration, 10903 New Hampshire Ave, WO62, Room 2114, Silver Spring, MD 20993 (K.A.W.); Biocoustics Research Laboratory, Department of Electrical and Computer Engineering, University of Illinois at Urbana-Champaign, Urbana, Ill (A.H.); Department of Radiology, University of Michigan, Ann Arbor, Mich (J.M.R.); Ultrasound Research and Education, Rocky Vista University, Ivins, Utah (J.G.); Department of Engineering, Pontificia Universidad Católica del Perú, Lima, Peru (R.L.); Laboratory of Biorheology and Medical Ultrasonics, University of Montreal Hospital Research Center, Montreal, Canada (G.C.); Institute of Cancer Research and Royal Marsden NHS Foundation Trust, Division of Radiotherapy and Imaging, Joint Department of Physics, London, UK (J.B.); and Pfizer, Cambridge, Mass (T.T.). Received March 31, 2022; revision requested May 23; revision received June 9; accepted July 8. **Address correspondence to** K.A.W. (email: [Keith.Wear@fda.hhs.gov](mailto:Keith.Wear@fda.hhs.gov)).

Conflicts of interest are listed at the end of this article.

Radiology 2022; 305:526–537 • <https://doi.org/10.1148/radiol.220606> • Content codes: **GI** **US**

Nonalcoholic fatty liver disease (NAFLD) is believed to affect one-third of American adults. Noninvasive methods that enable detection and monitoring of NAFLD have the potential for great public health benefits. Because of its low cost, portability, and noninvasiveness, US is an attractive alternative to both biopsy and MRI in the assessment of liver steatosis. NAFLD is qualitatively associated with enhanced B-mode US echogenicity, but visual measures of B-mode echogenicity are negatively affected by interobserver variability. Alternatively, quantitative backscatter parameters, including the hepatorenal index and backscatter coefficient, are being investigated with the goal of improving US-based characterization of NAFLD. The American Institute of Ultrasound in Medicine and Radiological Society of North America Quantitative Imaging Biomarkers Alliance are working to standardize US acquisition protocols and data analysis methods to improve the diagnostic performance of the backscatter coefficient in liver fat assessment. This review article explains the science and clinical evidence underlying backscatter for liver fat assessment. Recommendations for data collection are discussed, with the aim of minimizing potential confounding effects associated with technical and biologic variables.

© RSNA, 2022

**N**onalcoholic fatty liver disease (NAFLD) is the most common chronic liver condition in Western countries, due in large part to its association with type 2 diabetes, obesity, and metabolic syndrome. It is continuously increasing in incidence in both obese and nonobese populations worldwide (1). NAFLD can progress from simple steatosis to inflammation (steatohepatitis) to fibrosis to cirrhosis, which can require liver transplantation (2). Unfortunately, fatty liver disease is difficult to diagnose due to a lack of clinical symptoms in early stages of the disease, when steatosis remains reversible. Biochemical markers (liver function tests) are not accurate indicators for reflecting fat accumulation in hepatocytes (3). NAFLD strongly increases the risk of diabetes mellitus and cardiovascular disease (4). Quantitative biologic markers are urgently needed to detect early-stage NAFLD, quantify steatosis severity, assess treatment response, monitor disease progression, and predict treatment outcomes.

## AIUM–RSNA QIBA Efforts for US Liver Fat Quantification

The American Institute of Ultrasound in Medicine–Radiological Society of North America Quantitative Imaging Biomarkers Alliance (QIBA) Pulse-Echo Quantitative Ultrasound (PEQUS) Biomarker Committee was created in 2020 to develop and standardize protocols to quantify liver fat content using measurements that can be performed with clinical US imaging systems. The PEQUS Biomarker Committee includes dozens of physicians, scientists, and engineers (from academia, industry, and gov-

ernment) and is investigating three biologic markers to characterize liver fat: attenuation coefficient (AC), backscatter coefficient (BSC), and speed of sound. This article explains the science and clinical data behind BSC. While each of the three biologic markers has been used individually to assess liver fat with promising initial results, the committee is also exploring combinations of AC, BSC, and speed of sound (eg, linear combinations or artificial intelligence networks), which are anticipated to yield better diagnostic performance than any individual biologic marker. QIBA previously demonstrated a method with minimal cross-platform dependence for shear-wave elastography to characterize liver fibrosis (5). A glossary of terms used in this review is provided in Table 1.

## Methods for Liver Fat Assessment

### Biopsy

Currently, liver biopsy is still the accepted clinical reference standard in the diagnosis of nonalcoholic steatohepatitis. Biopsy involves direct visualization of histology with quantitative scoring on a four-point scale (range, 0–3) assessed from the percentage of parenchymal involvement by steatosis. However, biopsy has major limitations. First, biopsy is invasive and has a nonzero complication rate (6). Second, each liver biopsy samples only 1/50 000 of the liver mass (6), which can give an inadequate depiction considering that 10%–15% of fatty livers are inhomogeneous (7). Third, although the criteria for different degrees of fatty livers are well defined (eg, simple steatosis, parenchymal inflammation, hepatocyte ballooning,

## Abbreviations

AC = attenuation coefficient, BSC = backscatter coefficient, HRI = hepatorenal index, NAFLD = nonalcoholic fatty liver disease, NLV = normalized local variance, PDFF = proton density fat fraction, QIBA = Quantitative Imaging Biomarkers Alliance, RF = radiofrequency, ROI = region of interest

## Summary

Quantitative US backscatter shows promise in the noninvasive assessment of liver fat content but requires further protocol standardization and validation before widespread implementation in clinical care and research.

## Essentials

- B-mode US echogenicity of the liver is positively correlated with fat content.
- The hepatorenal index (HRI) and backscatter coefficient (BSC) (both of which are related to liver echogenicity) can be used to detect and assess liver steatosis.
- The BSC is expected to be less affected by confounding parameters (eg, tissue attenuation, machine gain settings, and transducer focusing) than the HRI.
- The American Institute of Ultrasound in Medicine and Radiological Society of North America Quantitative Imaging Biomarkers Alliance are working to standardize US acquisition protocols and data analysis methods to improve the diagnostic performance of BSC in liver fat assessment.

fibrosis associated with increased fat content or steatohepatitis [7]), interpretation by pathologists can be inconsistent (8). Therefore, physicians, other health care providers, patients, and researchers need a safer and more robust method with which to diagnose and monitor NAFLD.

## MRI-based Methods

MRI-based proton density fat fraction (PDFF) is well recognized as a reliable biologic marker with which to quantify fat accumulation in the liver. MRI PDFF findings have shown a close correlation with histology results ( $r = 0.85$ ) in the assessment of hepatic steatosis severity by measuring the percentage of mobile fat protons as compared with the total number of mobile protons (9). By sampling the entire liver, it has yielded within-subject reproducibility (SD) of less than 1% (10). Importantly, it is considered a reliable reference standard for other quantitative imaging biologic marker studies of NAFLD when liver histology results are unavailable (11). Further, MRI PDFF has been shown to be a useful measure of liver fat content in the assessment of treatment response in early-phase nonalcoholic steatohepatitis clinical trials (12). MR spectroscopy has also been used for liver fat quantification (13), but it is not as widely available as MRI PDFF. Limitations of MRI-based methods in screening for NAFLD include poor portability, high cost, and being contraindicated in patients with claustrophobia or implanted devices (eg, pacemakers) that are not compatible with MRI.

## B-Mode US

As discussed in a companion article (14), conventional B-mode US is commonly used to screen for liver steatosis (15), but the

high interobserver variability deters diagnosis (16). Standard visual B-mode US evaluation of fatty liver is mainly focused on changes in backscatter and attenuation compared with normal liver (15). Fat accumulation tends to result in greater backscatter from the liver parenchyma. Fat has a different acoustic impedance (product of density and sound speed; see Table 1 and the Basic Physics of Scattering section) than other liver tissue, so fat globules scatter (ie, redirect) ultrasound waves and thereby lead to higher echogenicity of fatty liver. Visual methods to assess steatosis are typically subjective. These can include scoring of liver echogenicity and loss or blurring of margins of typically bright intrahepatic structures, such as portal triads. Blurring is a consequence of spatial resolution degradation that arises from beam attenuation and phase aberration (beam distortion due to spatially heterogeneous sound speed; fat droplets have lower sound speed than surrounding tissue). These evaluations can be strongly influenced by transducer frequency, focusing properties, and machine settings (eg, nonlinear gray-scale maps) (17).

## US Attenuation

As a ultrasound beam propagates through tissues, it loses intensity due to attenuation, which is the combined result of absorption (conversion of US energy into heat) and scattering (redirection of incident ultrasound beam). In B-mode US, structures with low attenuation (eg, cysts) are responsible for distal enhancement, while structures with high attenuation (eg, calcium, stones, or gas) are responsible for distal shadowing (18). The AC can be measured by computer processing of radiofrequency (RF) signals received by the US transducer (19,20). (The RF signal is a digitized preprocessed signal that is also used to compute the brightness displayed on B-mode US images.) By comparing RF signals from regions at two different depths, the attenuation due to tissue between the two regions may be measured if system effects are properly accounted for. Since the AC is frequency dependent, this comparison is often done as a function of frequency in the frequency domain (eg, by computing Fourier transforms of RF signals) in decibels per centimeter. The AC may be reported (in decibels per centimeter) at a particular frequency or as a function of frequency. The rate of change of AC with frequency may be reported in decibels per centimeter per megahertz (also known as AC slope).

The clinical value of AC for quantification of liver steatosis is covered in a companion article (14). Attenuation measurement is available on several commercial US scanners. Multiple clinical studies have shown that attenuation parameters relate to MRI PDFF, suggesting that these parameters could be used to assess steatosis severity (7,14).

## US HRI

The hepatorenal index (HRI) is the ratio of mean image brightness in a liver region of interest (ROI) to mean image brightness in a nearby right kidney cortex ROI (21,22). Table 2 shows a summary of HRI measurements to diagnose hepatic steatosis in 13 clinical trials (21–33). Combined performance may be summarized by sensitivity (mean, 78%  $\pm$  22 [SD]), specificity (mean, 91%  $\pm$  12), and area under the

**Table 1: Glossary of Terms**

Term	Definition
Acoustic impedance	Product of density and sound speed; spatial variations in acoustic impedance result in scattering of incident US waves
AC	Quantitative index of the rate at which US waves lose energy due to absorption and scattering as they propagate through tissue (measured in decibels per centimeter)
AC slope	The rate at which AC varies with US frequency (measured in decibels per centimeter per megahertz)
B mode	Conventional US gray-scale image mode
BSC	Quantitative index of the fraction of incident US energy that gets redirected back toward the source transducer (1/cm-Sr or dB/cm-Sr) when tissue contains a spatial distribution of scatterers smaller than or on the order of a wavelength
Echogenicity	Gray-level brightness of tissue on a B-mode image
Elevational beam width	Width of the ultrasound beam perpendicular to the image plane
HRI	Ratio of mean gray-scale pixel values in liver ROI versus renal cortex ROI
Lateral beam width	Width of the ultrasound beam in the image plane
MRI PDFF	MRI-based biomarker for quantification of fat accumulation in the liver, expressed as an absolute percentage
NLV	Ratio of the variance to the squared mean of pixel gray levels in an ROI multiplied by $\pi/(4-\pi)$ (61)
Resolution volume	A volume below which a US system is unable to resolve structures, defined by the product of the pulse length, lateral beamwidth, and elevational beam width
RF	Digitized raw preprocessed signal obtained from US echoes that may be used to compute AC, BSC, or image brightness from ROI
Reference phantom method	Method for measuring AC and BSC simultaneously by comparing measurements from tissue to measurements from phantom with known AC and BSC
ROI	ROI on an image to isolate specific tissue for quantitative analysis
Speckle	Seemingly random pattern of bright and dark spots on an image resulting from constructive and destructive interference of waves scattered from multiple unresolvable structures
Specular reflection	US energy redirected by structures that are large relative to a wavelength or beam diameter
TSI-p	Gray-level brightness histogram shape parameter that is thought to indicate concentration and degree of regularity of scatterer spacing (64)
UDFF	Result of a least-squares model (based on correlation analysis of AC in dB/cm-MHz and BSC in dB/cm-Sr vs MRI-PDFF) that best predicts MRI PDFF in vivo (66)

Note—AC = attenuation coefficient, BSC = backscatter coefficient, HRI = hepatorenal index, NLV = normalized local variance, PDFF = proton density fat fraction, RF = radiofrequency, ROI = region of interest, TSI-p = tissue scatter distribution imaging parameter, UDFF = US-derived fat fraction.

**Table 2: Summary of Hepatorenal Index Measurements in the Diagnosis of Hepatic Steatosis (>5%) in Clinical Trials**

First Author, Year of Publication, and Reference No.	Sample Size	Sample Age (y)	Cutoff	Sensitivity (%)	Specificity (%)	AUC	Reference Standard
Webb, 2009 (21)	111	44 ± 12*	1.49	100	91	0.992	Biopsy
Mancini, 2009 (22)	40	28–65†	2.2	100	95	0.996	MR spectroscopy
Marshall, 2012 (23)	101	19–87†	1.28	100	54	0.92	Biopsy
Borges, 2013 (24)	42	18–70†	1.24	92.7	92.5	0.96	Biopsy
Martin-Rodriguez, 2013 (25)	121	21–77†	1.28	94.7	95.7	0.991	MR spectroscopy
Chauhan, 2016 (26)	45	24–76†	2.01	62.5	95.2	0.79	Biopsy
Moret, 2020 (27)	276	58 ± 11*	1.22	76.4	93.2	0.896	Biopsy
Petzold, 2020 (28)	157	48 ± 15*	1.46	42.7	90.7	0.68	Biopsy
Tanpowpong, 2020 (29)	179	23–77†	1.18	90	80	0.926	MRI PDFF
Johnson, 2021 (30)	267	52 ± 13*	1.17	64	97	...	Biopsy
Tran, 2021 (31)	52	32 ± 7*	1.54	50	91.7	0.74	MR spectroscopy
Kjaergaard, 2022 (32)	137	53–65†	1.46	48	100	0.79	Biopsy
Pirmoazen, 2022 (33)	31	52 ± 15*	2.24	94	100	1.00	MRI PDFF
Overall*	120 ± 83	...	1.52 ± 0.38	78 ± 22	91 ± 12	0.89 ± 0.11	...

Note—Another reference (99) analyzed a data set highly overlapping with the data set of Marshall et al (23), using a different analysis method. AUC = area under the receiver operating characteristic curve, PDFF = proton density fat fraction.

\* Data are mean ± SD.

† Data are the range.



**Figure 1:** B-mode US image of liver with steatosis grade S0 (<5%) and hepatorenal index (B ratio) of 1.00.



**Figure 3:** B-mode US image of liver with steatosis grade S0 (<5%) and hepatorenal index of 0.72.



**Figure 2:** B-mode US image of liver with steatosis grade S3 (≥66%) and hepatorenal index (B ratio) of 1.95.

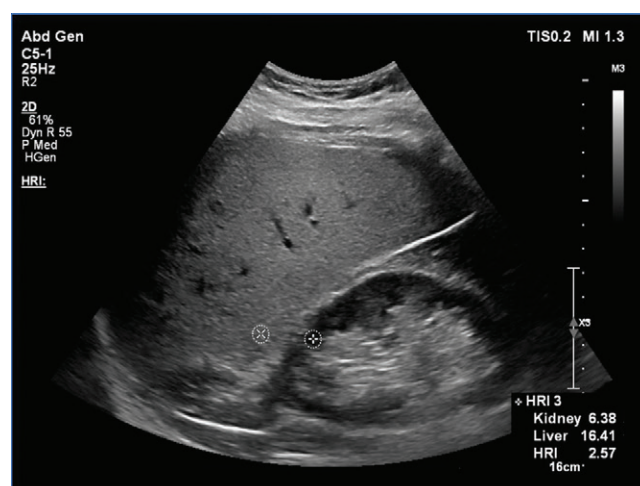


**Figure 4:** B-mode US image of liver with elevated steatosis grade and hepatorenal index of 2.57.

receiver operating characteristic curve (mean,  $0.89 \pm 0.11$ ). However, the variability in optimal HRI cutoff levels in these studies was considerable, as noted previously (14,34), ranging from 1.17 to 2.24 (mean,  $1.5 \pm 0.4$ ), suggesting inferior average performance might be expected if one HRI cutoff level was used for all studies. Further, all trials used one scanner, so intersystem variability was not tested. Figures 1–5 show measurements of HRI from B-mode US images in livers with normal and elevated steatosis grades.

#### Limitations of US HRI in the Diagnosis of Hepatic Steatosis

The necessity of the right kidney as a reference can be problematic because HRI measurements can be compromised in patients with (a) severe renal cortical scarring, (b) incidental large or numerous renal cysts or solid mass lesions, (c) hydronephrosis, or (d) lack of one image containing both the liver and the right kidney (23,26). The HRI may be confounded by concomitant fibrosis (35) and by differences in beam focusing and intervening attenuation between the transducer and the two ROIs. A further limitation of HRI is that, due to anisot-

ropy of backscattering from the kidney (36,37), the reference measurement depends on the angle at which US interrogates the kidney. Finally, operator-dependent variation in placement of ROIs can add variability to HRI.

HRI measurement capability is currently offered on several commercial platforms. Alternatively, HRI can be measured offline from images acquired with any system by using image analysis tools that are commonly available in picture archiving and communications system software. Numeric values of HRI, and hence cutoff values, may be influenced by nonlinear signal processing, such as dynamic range compression. (To display weakly scattering structures, such as blood, and strongly scattering structures, such as fluid-tissue interfaces, on the same image, US echo amplitudes are sometimes compressed by applying nonlinear operators, such as logarithms. Nonlinear signal processing disrupts the approximately proportional relationship between image gray level and backscatter strength. Therefore, HRI and cutoff values may vary depending on the details of the nonlinear compression method.)

## US BSC

## Basic Physics of Scattering

When an ultrasound beam propagates through tissue and encounters a spatial variation (on a scale smaller than or on the order of a wavelength) in local acoustic impedance (Table 1), a



**Figure 5:** B-mode US image of liver with elevated steatosis grade and hepatorenal index of 2.57.

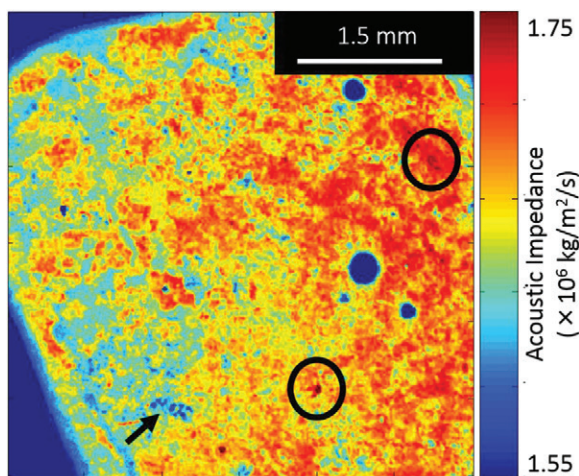


**Figure 6:** Acoustic micrograph acquired at 80 MHz shows two-dimensional acoustic impedance distribution of nonalcoholic steatohepatitis in mouse liver. Black circles indicate patterns of higher-than-normal acoustic impedance values. Black arrow points to an area with lower-than-normal impedance values. (Reprinted, with permission, from reference 38.)

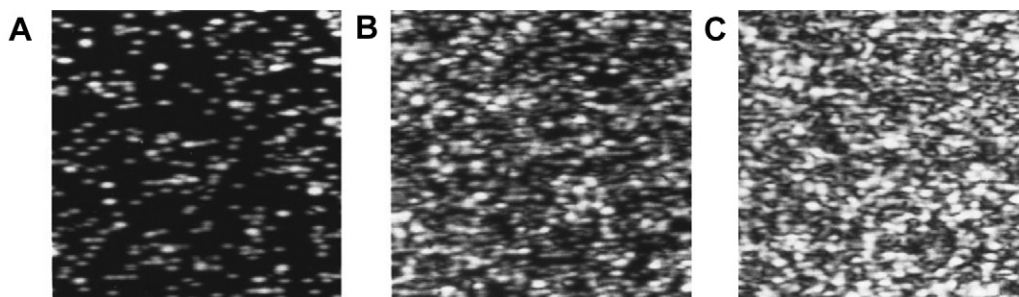


**Figure 7:** B-mode US images generated with computer simulation. The numbers of scatterers per spatial resolution volume are (A) less than 1, (B) equal to 2, and (C) equal to 6. (Reprinted, with permission, from reference 41.)

fraction of the incident US energy is scattered in all directions. (Scattering is distinguished from US energy redirected  $180^\circ$  by a structure much larger than a wavelength, which is called specular reflection.) The portion of scattered US energy redirected by  $180^\circ$  (ie, backward, toward the US source) is called backscatter. Foreexample, fat has 10% lower density ( $\rho$ ) than water (eg,  $0.9 \text{ g/cm}^3$  vs  $0.997 \text{ g/cm}^3$ ) and 6% slower speed of sound ( $c$ ) than water (eg,  $1450 \text{ m/sec}$  vs  $1540 \text{ m/sec}$ ), resulting in an impedance ( $\rho c$ ) mismatch between lipid vacuoles and water-based cytoplasm of approximately 16%. Therefore, lipid vacuoles scatter ultrasound and lead to a higher BSC of fatty liver. Figure 6 shows the acoustic microstructure in a mouse liver with nonalcoholic steatohepatitis (38). The liver exhibits much microstructural variation in acoustic impedance throughout a typical clinical (3-MHz) spatial resolution volume, which is the product of the US pulse length in the propagation direction (about 1.5 times the wavelength, or  $750 \mu\text{m}$ ), the lateral (ie, in the image plane) beam width (a few millimeters), and the elevational (ie, perpendicular to the image plane) beam width (a few millimeters).

As discussed in the Positioning Transducer and ROI section of this article, backscatter data are usually acquired from regions not containing resolvable structures, such as larger blood vessels, bile ducts, portal tracts, or focal lesions. In these regions, backscatter from the liver may be attributed to many distributed unresolvable structures. The unresolved component appears on the B-mode US display as a pattern of bright and dark spots, known as speckle (39,40). The gray levels of the spots are related to magnitudes of impedance mismatches at scattering interfaces, the effective numbers of contributing scatterers, and the degree to which scattered waves interfere constructively (ie, in phase) or destructively (ie, out of phase). Figure 7 shows that speckle patterns develop when the number of scatterers per spatial resolution volume is high enough. Theoretically, when the effective number of scatterers per spatial resolution volume is less than or equal to one, then (assuming that echoes from single scatterers are strong enough to be detected) individual spots correspond to individual scatterers, but there is no speckle (Fig 7A). However, if the effective number of scatterers per spatial resolution volume is greater than one (as is the case with the liver), then individual spots result from interferences of waves scattered by multiple structures contained within a spatial resolution volume (41) (Fig 7C). When scattering structures are much smaller than the spatial resolution volume, the sizes of and distances between speckle spots are determined by the spatial resolution limitations

of the US imaging system rather than by the scatterer sizes.

Backscatter from a volume of tissue containing many distributed unresolvable scatterers (eg, liver) may be quantified by BSC, which is measured in units of  $1/\text{centimeter-steradian}$  (hereafter,  $1/\text{cm-Sr}$ ). The units arise from the effective number

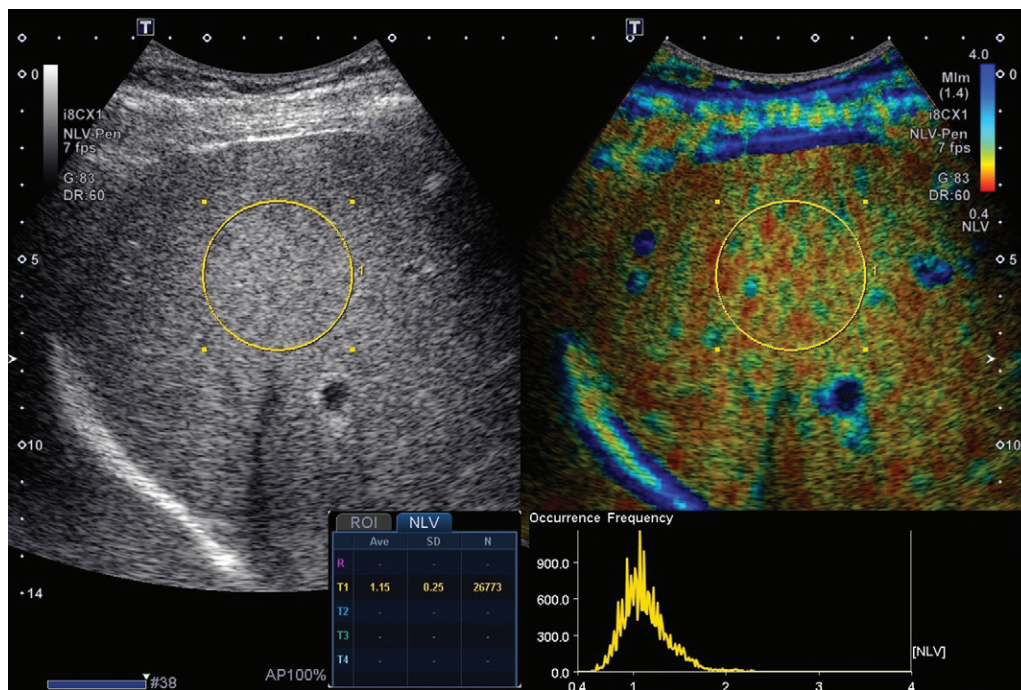


**Figure 8:** B-mode gray-level histogram analysis from liver of patient with a proton density fat fraction of 3.6%. Left: B-mode gray-level image. Yellow circle indicates region of interest. Right: Normalized local variance (NLV) image. Red and blue indicate lower and higher NLV values, respectively.

of scatterers per unit volume (in inverse cubic centimeters) multiplied by the average scatterer cross section (in square centimeters) redirecting incident ultrasound into a solid angle (measured in steradians) centered around  $180^\circ$ . The BSC is a primary determinant of gray-scale brightness on a B-mode US image in regions of tissues containing diffuse scatterers.

Additional information regarding scatterer sizes can be obtained from frequency domain analysis of RF backscattered signals (37,42–56). Information regarding spatial distributions of scatterers, including number of scatterers per spatial resolution volume and regularity of scatterer spacing, can be inferred from statistical distributions (eg, histograms) of brightness levels (55,57–59). The underlying theory is very mathematical and beyond the scope of this review. To our knowledge, detailed connections between histogram shapes and liver histology results have not been confirmed. Heterogeneity and spatial correlations among scatterers can affect the histogram shape (57,59,60), which has been assessed with commercial scanners by using the normalized local variance (NLV) (61,62) and the tissue scatter-distribution imaging parameter (63,64). As shown in Figures 8 and 9, NLV, which is thought to indicate heterogeneity of dominant scattering structures, has been used to assess steatosis (7,61,62). In fatty liver, scattering is thought to be dominated by relatively homogenous scatterers within the parenchyma, resulting in an NLV value close to one, indicative of a Rayleigh-distributed histogram (61,62). In normal livers, scattering from parenchyma is diminished, so echo amplitudes are due to comparable contributions from parenchyma and small-vessel walls, collectively appearing as a heterogeneous set of scatterers, increasing the variance relative to the mean squared, resulting in an

NLV value different from one (61,62). The tissue scatter distribution imaging parameter, which is thought to indicate concentration and degree of regularity of scatterer spacing (63,64), has also been used to assess steatosis (64). Histogram shape parameters have a complex dependence on the size of the system spatial resolution volume, creating formidable challenges for system-independent measurements.

### Reference Phantom Method for Clinical Measurement of BSC

The reference phantom method enables accurate measurement of BSC that is independent of machine factors (eg, gain settings, beam focusing

properties) (65). The method is performed as follows: Gain settings (eg, transmit level and depth gain compensation) are optimized for the individual patient. Then, an ROI within the liver is marked for analysis. RF data (before nonlinear compression) are acquired from the ROI. Next, with the same gain and ROI settings, data are acquired from a reference (calibration) phantom in which AC and BSC previously have been measured (eg, by the manufacturer). When RF backscatter spectral ratios are taken between patient and phantom measurements, the effects of gain and beam focusing cancel out, enabling system-independent BSC measurements, which are presented schematically elsewhere, to be obtained (56). For AC, as was discussed earlier in this article, this analysis is typically performed in the frequency domain (ie, after Fourier transforms of RF waveforms) because both AC and BSC are functions of frequency. A database of reference phantom measurements with a variety of gain settings and ROI sizes and locations may be acquired in advance by the manufacturer, as is done in one commercial implementation (66), to facilitate real-time online data analysis and to make phantom data acquisition unnecessary at the time of patient examination.

### BSC Measurements in Normal and Fatty Livers

As shown in Table 3, early investigations established feasibility of BSC measurements in vitro from tissue samples (67,68). Subsequent clinical investigations measured a normal range of liver BSC in vivo of about  $(4 \pm 2) \times 10^{-4}$  1/cm-Sr, based on examinations of groups of 13–35 participants (children and adults) at frequencies ranging from 2.25 MHz (69) to 3 MHz (70,71). In one of these investigations, fatty infiltration in

seven participants elevated the mean BSC by a factor of 17, to a level of  $(68 \pm 37) \times 10^{-4}$  1/cm-Sr at 3 MHz (71). One early in vivo study (69) used image gray-scale data, while two early in vivo studies (70,71) used RF data. RF data are preferred for accurate frequency domain compensation for machine settings, transducer properties, and beam propagation (65). RF data also allow the frequency dependence of the BSC to be determined. For example, although a transducer might have a nominal frequency of 3 MHz, it actually transmits ultrasound waves at frequencies throughout a range, such as 2.5–3.5 MHz. Frequency-domain processing allows assessment of how BSC varies throughout this frequency range. Since the BSC for fatty liver rises more rapidly with frequency than the BSC for normal liver (67), the BSC slope (1/cm-Sr/MHz) might be a further biologic marker of steatosis since it would be expected to be positively correlated with fat content in the liver. However, BSC slope might be impractical in obese patients with high liver attenuation and poor backscatter signal quality.

**Relationship between BSC and MRI PDFF in Clinical Trials**

Recently, BSC has been investigated in larger clinical trials. Figure 10 shows

measurements of AC and BSC in patients with three grades of steatosis. In a prospective cross-sectional study of 204 adults, 140 with NAFLD (MRI PDFF  $\geq 5\%$ ) and 64 without NAFLD (MRI PDFF  $< 5\%$ ), BSC at 3 MHz correlated with MRI PDFF, with a Spearman rank correlation coefficient of 0.80 (72). In the detection of steatosis with BSC, sensitivity was 87% (95% CI: 77, 94), specificity was 91% (95% CI: 75, 98), and area under the receiver operating characteristic curve was 0.95 (95% CI: 0.90, 1.00).

In another study of 102 adults (78 with NAFLD [MRI PDFF  $\geq 5\%$ ]), BSC and AC at 2.7 MHz had Pearson



**Figure 9:** B-mode gray-level histogram analysis from the liver of a patient with proton density fat fraction of 20.5%. Left: B-mode gray-level image. Yellow circle indicates region of interest. Right: Normalized local variance (NLV) image. Red and blue indicate lower and higher NLV values, respectively.

**Table 3: Summary of Backscatter Coefficient Measurements in the Liver in the 2–3-MHz Frequency Range**

First Author, Year of Publication, and Reference No.	Frequency (MHz)	In Vitro or in Vivo	Sample Size	Liver State	BSC (1/cm-Sr $\times 10^{-4}$ )*
Bamber, 1981 (67)	2.5	In vitro	17	Normal	$2.5 \pm 2.0$
Nicholas, 1982 (68)	3	In vitro	Not provided	Normal	$9 \geq 2.0$
O'Donnell, 1985 (69)	2.25	In vivo	13	Normal	$3.5 \geq 1.2^\dagger$
Wear, 1995 (70)	3	In vivo	15	Normal	$2.9 \geq 1.8$
Lu, 1999 (71)	3	In vivo	35	Normal	$5 \geq 2.0$
Lu, 1999 (71)	3	In vivo	7	Fatty infiltration	$68 \geq 37$
Lin, 2015 (72)	3	In vivo	204	MRI PDFF 11.1% $\geq 8.6^*$	$22 \geq 38$
Paige, 2017 (81)	3	In vivo	60	MRI PDFF 15.0% $\geq 9.0^{*\ddagger}$	$380 \geq 640^\ddagger$
Han, 2020 (73)	2.7	In vivo	102	MRI PDFF 12.8% $\geq 8.8^*$	$45 \geq 55$

Notes— BSC = backscatter coefficient, PDFF = proton density fat fraction.

\* Data are mean  $\geq$  SD.

† All measurements were based on radiofrequency data, except O'Donnell and Reilly, 1985, which used envelope-detected data.

‡ Histology-confirmed steatosis grades were S1 (n = 27), S2 (n = 16), and S3 (n = 17). In this study, BSC values were much higher because all patients had histologically confirmed nonalcoholic fatty liver disease.

correlation coefficients of 0.58 and 0.59, respectively, with MRI PDFF (73). Combining multiple quantitative US parameters yielded a fat fraction estimate with a Spearman rank correlation coefficient of 0.82 and a Pearson correlation coefficient of 0.76 with MRI PDFF.

In a study of 101 adults (66) (a portion of which overlapped with the previously mentioned study [73], 93 with NAFLD [MRI PDFF  $\geq 5\%$ ]) in which a commercial scanner was used, a least-squares fit of a quadratic function to MRI PDFF versus BSC at 3 MHz yielded a coefficient of determination ( $R^2 = 0.76$ ) that was higher than the coefficient of determination for MRI PDFF versus AC ( $R^2 = 0.6$ ). Log-transformed BSC and AC also were analyzed in least-squares models to evaluate correlations with MRI PDFF. The model that best predicted MRI PDFF is called the US-derived fat fraction (UDFF). The Pearson correlation coefficient between UDFF and MRI PDFF was 0.87. For detection of steatosis with UDFF, sensitivity was 84% (95% CI: 76, 92), specificity was 100% (95% CI: 100, 100), and area under the receiver operating characteristic curve was 0.94 (95% CI: 0.85, 0.98). Figures 11 and 12 show measurements of UDFF in normal and fatty livers.

## Accuracy, Precision, Repeatability, and Reproducibility of BSC in Liver

### Technical Confounders

Repeatability is “the measurement precision with conditions that remain unchanged between replicate measurements,” whereas reproducibility is “the measurement precision with conditions that vary between replicate measurements” (74).

Variability in BSC estimates is impacted by the random nature of wave interference (75) and heterogeneity of liver tissue. The accuracy of the reference phantom method has been validated in interlaboratory studies against rigorous experimental laboratory methods for measuring BSC (76,77). Cross-platform reproducibility (SD) of BSC has been measured at typically about 1 dB (26%) in phantoms between 1 and 12 MHz (78,79) and somewhat higher in rodent fibroadenomas between 3.9 and 4.9 MHz (80). These values are small compared with the range of BSC in normal and fatty livers. For example, one study reported a liver BSC range of 0.001–0.40 1/cm-Sr in adults with MRI PDFF ranging from 1.4% to 35.0% (81). This corresponds to  $10 \times \log_{10}(0.40/0.001)$ , which is equal to 26 dB.

In a study of 41 adults known to have or suspected of having NAFLD, the average within-participant BSC SD was 2.4 dB (82). The between-image repeatability was assessed under various measurement conditions (ie, sonographer-transducer-trial combinations), and the intraclass correlation coefficient estimate was greater than 0.9 for most conditions (82).

In a study of 61 adults known to have or suspected of having NAFLD, log-transformed BSC was very reproducible among six

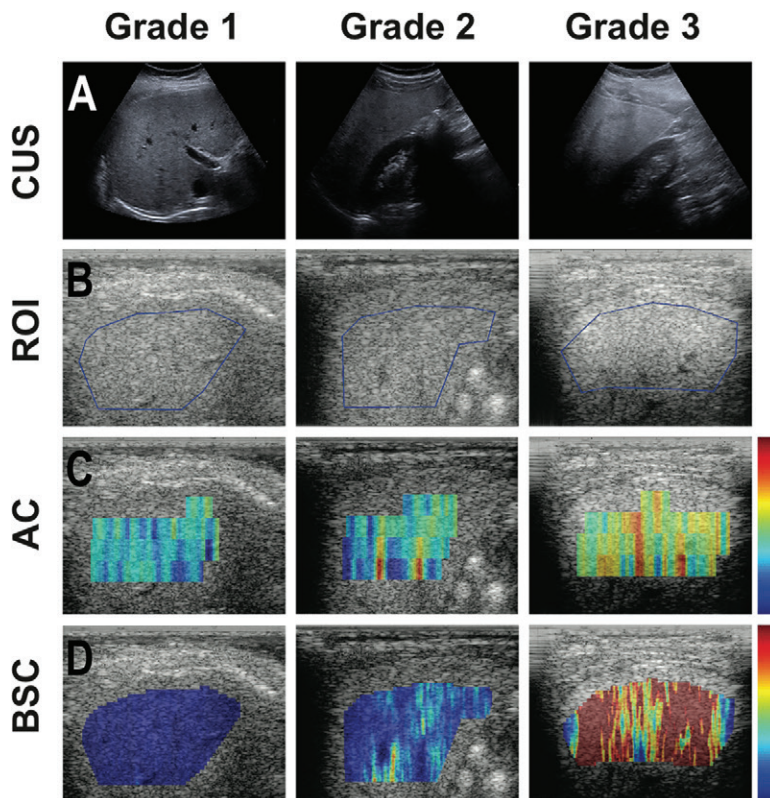


**Figure 10:** Three patients with grade 1 (36-year-old woman), grade 2 (27-year-old man), and grade 3 (22-year-old man) steatosis as determined by histologic examination. **(A)** Conventional US (CUS) B-mode images in each patient were used by radiologists for conventional scoring. **(B)** Quantitative US images in the same three patients. Blue outline shows fields of interest, as determined by one study image analyst. **(C, D)** Parametric color-coded maps for attenuation coefficient (range, 0–2 dB/cm-MHz) **(C)** and backscatter coefficient (range, 0–0.25 1/cm-Sr) **(D)**. Red indicates higher values and blue indicates lower values. AC = attenuation coefficient, BSC = backscatter coefficient, ROI = region of interest. [Reprinted, with permission, from reference 81.]

sonographers, with an intersonographer intraclass correlation coefficient of 0.87 (95% CI: 0.78, 0.92) or 0.88 (95% CI: 0.80, 0.93) for estimates obtained from one or five quantitative US acquisitions, respectively (83).

In a study of 64 adults known to have or suspected of having NAFLD, the interplatform intraclass correlation coefficient was 0.70 for log-transformed BSC in terms of absolute agreement (84). Pearson correlation coefficient of the log-transformed BSCs between two platforms was 0.80.

### Biologic Confounders

In a study of 83 adults with results of histologic analysis, no confounding effect of either liver fibrosis or lobular inflammation was observed (73). BSC of the cirrhotic liver does not differ significantly from BSC of the healthy liver (71). In a study of 41 adults known to have or suspected of having NAFLD, BSC demonstrated minimal correlation with body mass index (82). It is unknown if the glycogen content of the liver is a confounder for BSC measurement, although glycogen may have a major time-varying effect on AC (85,86).

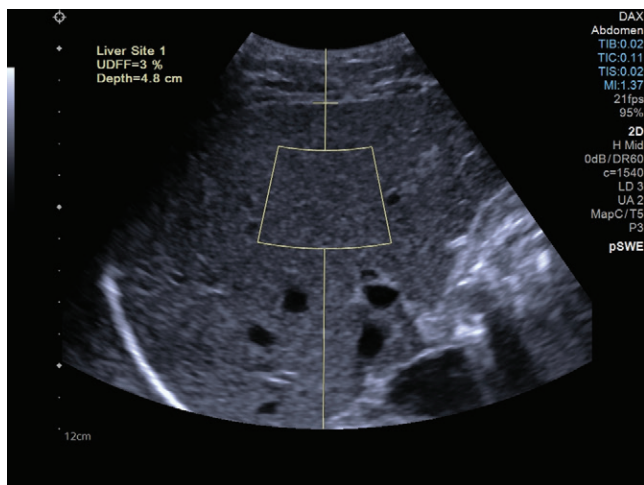


**Figure 11:** B-mode US image of liver with a US-derived fat fraction (UDFF) of 3% and an MRI protein density fat fraction of 3%.

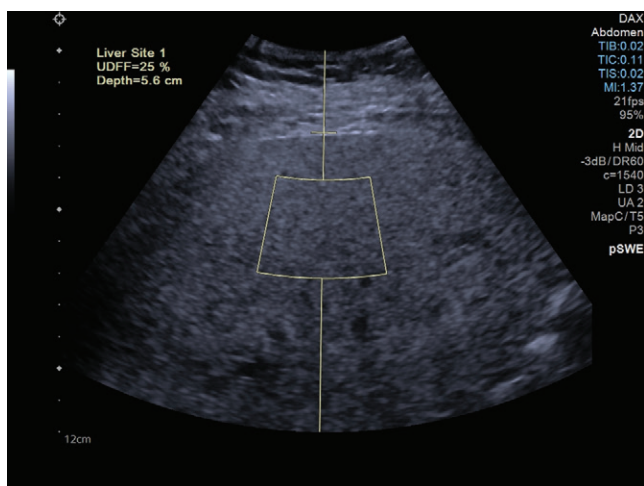


**Figure 12:** B-mode US image of liver with a US-derived fat fraction (UDFF) of 25% and an MRI protein density fat fraction of 25%.

## Toward Standardization of Clinical BSC Measurements in Liver

### Patient Preparation

The importance of fasting prior to liver backscatter measurements is not known. Fasting for at least 4 hours before shear-wave elastography measurement is recommended because ingestion of food stimulates more blood flow to the liver, which results in increased shear stiffness (87). The effect of blood flow–related shear stiffness changes on backscatter is not known. However, backscatter depends on scatterer number density, and shear stiffness is increased by blood flow–related prestress and liver expansion (which could affect scatterer number density). Therefore, backscatter measurements could be affected by bulk stiffness changes, although perhaps not as much as shear-wave elastography measurements.

### Positioning Transducer and ROI

It is probably advisable to follow recommendations devised for US elastography of the liver. Measurements should be obtained

with an intercostal approach at the location of the best acoustic window (88). The ultrasound beam should be as close to perpendicular to the liver capsule as possible (88). Bile ducts, blood vessels, portal tracts, focal lesions, rib shadows, and reverberations from the liver capsule should be avoided (88,89).

### Data Acquisition

Performing averaging over repeated measurements is expected to reduce measurement variance. Ten independent measurements per patient are recommended for shear-wave elastography (90). Fewer measurements might be sufficient for BSC (83), but this requires further study. Separating data acquisitions by breath holds might improve reliability. Breath holds may be more important for shear-wave elastography however, because shear-wave velocity measurements are based on the subtle motion of tissue in response to acoustic radiation force impulse beams. Moving and rotating the transducer between acquisitions will likely improve the statistical independence of measurements and thus the robustness of the average BSC value.

### Compensation for Attenuation between the US Probe and Measurement ROI

Calculation of BSC requires compensation for the total attenuation of US by all intervening tissues between the body surface and the deepest point in the ROI in the liver. Since AC depends on frequency, attenuation compensation is usually performed by using US spectra (ie, Fourier transforms of RF data). Three approaches have been reported and are detailed in this section.

The first approach is individual tissue compensation. This approach relies on identification and measurement of tissue layers (ie, skin, muscle, fat, and liver) in the propagation path to the ROI (70,71,91). An AC value at each BSC measurement frequency is assigned to each tissue using representative values in the literature (92). The total attenuation is the sum of attenuation contributions from all tissues. However, the operator-dependent nature of abdominal wall annotation (93) and the inter-subject variability of ACs (especially in the presence of increased fat content) may affect the effectiveness of this approach.

The second approach is compensation based on one AC at each measurement frequency. This simplified approach does not account for the fact that components of the abdominal wall, such as fat and muscle, have markedly different values (eg, 1.8 dB/cm vs 3.6 dB/cm, respectively at 3 MHz) (92). Therefore, the choice of AC value could significantly influence the accuracy of BSC estimation. This approach has two main variations. The first variation uses a fixed AC at each frequency (eg, calculated from a linear AC versus frequency model and an AC slope of 0.9 dB/cm/MHz, which is the average of expected values for fat and muscle). This would result in worst case error magnitude at 3 MHz and a 5-cm depth of  $3 \text{ MHz} \times (2 \times 5 \text{ cm round trip}) \times 0.3 \text{ dB/cm/MHz} = 9 \text{ dB}$  in the extremely unlikely event that the abdominal wall is entirely composed of either fat or muscle. The second variation uses an estimate of the liver AC to compensate for the total attenuation (72,73,94). This would likely bias the estimated BSC due to the positive correlation of liver attenuation with fat content.

The third approach is parametric modeling and joint estimation of total attenuation and BSC. This approach relies on estimating both total attenuation and BSC from the measured frequency-dependent US spectra (95–98).

At present, all methods remain viable options. The use of an estimate of the liver AC to compensate for the total attenuation has been studied in the largest clinical trials and yields results that reflect the positive correlation of BSC with steatosis stage. When selecting a method, the primary objective is to measure an index that correlates as closely as possible with the fat fraction. A secondary objective is the ease of implementation. A third objective is to measure BSC as accurately as possible so that steatosis grades and cutoff values become translatable between systems. These objectives may not necessarily be mutually compatible.

### Reporting of BSC Values

BSC results are usually calculated as inverse centimeter-steradian and are reported as units of  $\times 10^{-4}$ /centimeter-steradian, but the log-transformed BSC has recently been reported in decibels, with 1/cm-Sr defined as the 0-dB reference (66,82). For consistency, the frequency at which BSC (or any parameter derived from BSC) is reported should be standardized, with 3 MHz being a typical frequency for the liver. A question also remains if this could also be converted into a fat fraction (using PDFF as the reference standard) to facilitate clinical interpretation. In addition to reporting the mean values of measurements, some measure of statistical uncertainty (eg, SD or IQR) should be reported.

### Conclusion

Quantitative US is promising in the assessment of liver steatosis and may be optimal in the screening of patients with or without symptoms because it is a safe and widely available technology for scanning regions of the liver that provide meaningful quantitative information. US is less invasive than biopsy and less expensive and more portable than MRI. Currently, there is more evidence to support attenuation than backscatter or sound speed for assessment of steatosis. However, backscatter and sound speed may be computed from the same US data set acquired for attenuation and may provide complementary diagnostic information. Comparisons between AC and BSC for assessment of steatosis are rare, but two studies suggest similar performance for the two parameters (73,81). Some studies suggest that log-transformed BSC might perform better than AC or BSC (73,81). One commercial implementation uses a least-squares model (based on correlation analysis of AC and BSC vs MRI PDFF) that has been optimized for assessment of steatosis (66).

US backscatter may be quantified by HRI and BSC. Many clinical studies have shown that HRI and BSC can be used to detect steatosis and assess liver fat content in adults suspected of having or known to have NAFLD and, with further validation, these biologic markers might be applicable in various contexts of use for clinical care, clinical trials, and research. HRI is simple to measure, can be implemented with existing technology, and can effectively reduce variability due to attenuation of overlying tissues if attenuation is similar for liver and kidney paths. However, HRI is negatively affected by intersystem variability, inconsistency of backscatter from the reference (kidney), and ambiguity

in cutoff values. Most data to support BSC have been acquired using research scanners, reference phantom measurements, and offline processing. However, one commercial implementation has shown that it is feasible to measure BSC with a clinical scanner providing immediate online processing in a user-specified ROI, without the need for a reference phantom measurement (by having previously acquired phantom data already stored in the system) (66). Based on the QIBA effort to develop standardized protocols and data analysis methods, it is anticipated that BSC measurement capability will be incorporated into more commercial clinical scanners.

Most clinical data to support effectiveness of HRI, BSC, and histogram parameters have been obtained using single systems. Unlike HRI and histogram parameters, BSC has been shown to exhibit minimal system dependence in extensive phantom and animal studies. This makes BSC suitable for QIBA standardization efforts.

Future directions that should be investigated include (a) parametric models and advanced algorithms to facilitate automated online simultaneous estimation of AC and BSC; (b) non-linearity between BSC versus MRI PDFF with saturation effects at MRI PDFF values greater than approximately 34% (73); (c) intersystem variability, measured using liver-mimicking phantoms (currently planned by QIBA); (d) performance of BSC in multicenter trials; (e) validation and FDA biologic marker qualification for various contexts of use; (f) translation to children; and (g) translation to handheld devices operated by nonexperts.

The American Institute of Ultrasound in Medicine and Radiological Society of North America Quantitative Imaging Biomarkers Alliance are building on existing clinical evidence to develop standardized US acquisition protocols and data analysis methods to improve the diagnostic performance of backscatter coefficient (BSC) in liver fat assessment. Careful attention to minimization of potential confounding effects of technical and biologic variables is expected to improve the clinical performance of BSC in liver fat assessment.

**Acknowledgments:** The authors thank the chairs of the Quantitative Imaging Biomarkers Alliance Pulse Echo Quantitative Ultrasound biomarker committee: Anthony Samir, MD, MPH, Massachusetts General Hospital, Harvard Medical School; Ivan Rosado-Mendez, PhD, University of Wisconsin Department of Medical Physics; and Michael Wang, PhD, General Electric Healthcare. The authors thank Shahram Vaezy, PhD, U.S. Food and Drug Administration, for providing helpful comments.

**Disclosures of conflicts of interest:** **K.A.W.** Technical support from Siemens; royalties from CIRS; patent issued; chair of AIUM Bioeffects Committee and AAPM Task Group 333 MR-guided Focused Ultrasound Quality Assurance. **A.H.** Member of the AIUM Bioeffects Committee. **J.M.R.** Consultant to Endra; consulting fees from Endra; support to attend meetings or travel from Endra; patents planned, issued, or pending from Endra; stock or stock options in Endra. **J.G.** Clinical research grants and US equipment from Canon Medical Systems, Endra Life Sciences, and Siemens Healthineers. **R.L.** Grant 150-2020-FONDECYT; VP Elect Member and Student Activities for Institute of Electrical and Electronics Engineers Engineering in Medicine and Biology Society. **G.C.** Institution was loaned two Siemens Sequoia US systems; institution received partial grant funding from Siemens Healthcare. **J.B.** Research grants in various areas, including staff and students, from Cancer Research UK, EPSRC, Institute of Cancer Research, University of Surrey, and Exact Therapeutics; honorarium for a lecture from Samsung Healthcare. **T.T.** Pfizer stock.

### References

1. Loomba R, Sanyal AJ. The global NAFLD epidemic. *Nat Rev Gastroenterol Hepatol* 2013;10(11):686–690.

2. Paik JM, Henry L, De Avila L, Younossi E, Racila A, Younossi ZM. Mortality Related to Nonalcoholic Fatty Liver Disease Is Increasing in the United States. *Hepatology Commun* 2019;3(11):1459–1471.
3. Udombap P, Kim D, Kim WR. Current and Future Burden of Chronic Nonmalignant Liver Disease. *Clin Gastroenterol Hepatol* 2015;13(12):2031–2041.
4. Anstee QM, Targher G, Day CP. Progression of NAFLD to diabetes mellitus, cardiovascular disease or cirrhosis. *Nat Rev Gastroenterol Hepatol* 2013;10(6):330–344.
5. Palmeri ML, Milkowski A, Barr R, et al. Radiological Society of North America/Quantitative Imaging Biomarker Alliance Shear Wave Speed Bias Quantification in Elastic and Viscoelastic Phantoms. *J Ultrasound Med* 2021;40(3):569–581.
6. Bravo AA, Sheth SG, Chopra S. Liver biopsy. *N Engl J Med* 2001;344(7):495–500.
7. Ferraioli G, Berzigotti A, Barr RG, et al. Quantification of Liver Fat Content with Ultrasound: A WFUMB Position Paper. *Ultrasound Med Biol* 2021;47(10):2803–2820.
8. Bedossa P; FLIP Pathology Consortium. Utility and appropriateness of the fatty liver inhibition of progression (FLIP) algorithm and steatosis, activity, and fibrosis (SAF) score in the evaluation of biopsies of nonalcoholic fatty liver disease. *Hepatology* 2014;60(2):565–575.
9. Kühn JP, Hernando D, Muñoz del Río A, et al. Effect of multipeak spectral modeling of fat for liver iron and fat quantification: correlation of biopsy with MR imaging results. *Radiology* 2012;265(1):133–142.
10. Yokoo T, Bydder M, Hamilton G, et al. Nonalcoholic fatty liver disease: diagnostic and fat-grading accuracy of low-flip-angle multiecho gradient-recalled-echo MR imaging at 1.5 T. *Radiology* 2009;251(1):67–76.
11. Ferraioli G, Maiocchi L, Raciti MV, et al. Detection of Liver Steatosis With a Novel Ultrasound-Based Technique: A Pilot Study Using MRI-Derived Proton Density Fat Fraction as the Gold Standard. *Clin Transl Gastroenterol* 2019;10(10):e00081.
12. Caussy C, Reeder SB, Sirlin CB, Loomba R. Noninvasive, Quantitative Assessment of Liver Fat by MRI-PDFF as an Endpoint in NASH Trials. *Hepatology* 2018;68(2):763–772.
13. Thomsen C, Becker U, Winkler K, Christoffersen P, Jensen M, Henriksen O. Quantification of liver fat using magnetic resonance spectroscopy. *Magn Reson Imaging* 1994;12(3):487–495.
14. Ferraioli G, Kumar V, Ozturk A, Nam K, de Korte CL, Barr RG. US Attenuation for Liver Fat Quantification: An AIUM-RSNA QIBA Pulse-Echo Quantitative Ultrasound Initiative. *Radiology* 2022;302(3):495–506.
15. Barr RG. Ultrasound of Diffuse Liver Disease Including Elastography. *Radiol Clin North Am* 2019;57(3):549–562.
16. Dasarthy S, Dasarthy J, Khiyami A, Joseph R, Lopez R, McCullough AJ. Validity of real time ultrasound in the diagnosis of hepatic steatosis: a prospective study. *J Hepatol* 2009;51(6):1061–1067.
17. Long Z, Zhou W, Tradup DJ, Stelkel SF, Callstrom MR, Hangiandreou NJ. Systematic optimization of ultrasound grayscale imaging presets and its application in abdominal scanning. *J Appl Clin Med Phys* 2020;21(10):192–199.
18. Rubin JM, Adler RS, Bude RO, Fowlkes JB, Carson PL. Clean and dirty shadowing at US: a reappraisal. *Radiology* 1991;181(1):231–236.
19. Fink M, Hottier F, Cardoso JF. Ultrasonic signal processing for in vivo attenuation measurement: short time Fourier analysis. *Ultrason Imaging* 1983;5(2):117–135.
20. Labyed Y, Bigelow TA. A theoretical comparison of attenuation measurement techniques from backscattered ultrasound echoes. *J Acoust Soc Am* 2011;129(4):2316–2324.
21. Webb M, Yeshua H, Zelber-Sagi S, et al. Diagnostic value of a computerized hepatorenal index for sonographic quantification of liver steatosis. *AJR Am J Roentgenol* 2009;192(4):909–914.
22. Mancini M, Prinster A, Annuzzi G, et al. Sonographic hepatic-renal ratio as indicator of hepatic steatosis: comparison with (1)H magnetic resonance spectroscopy. *Metabolism* 2009;58(12):1724–1730.
23. Marshall RH, Eissa M, Bluth EI, Gulotta PM, Davis NK. Hepatorenal index as an accurate, simple, and effective tool in screening for steatosis. *AJR Am J Roentgenol* 2012;199(5):997–1002.
24. Borges VF, Diniz AL, Cotrim HP, Rocha HL, Andrade NB. Sonographic hepatorenal ratio: a noninvasive method to diagnose nonalcoholic steatosis. *J Clin Ultrasound* 2013;41(1):18–25.
25. Martín-Rodríguez JL, Arrebola JP, Jiménez-Moleón JJ, Olea N, González-Calvin JL. Sonographic quantification of a hepato-renal index for the assessment of hepatic steatosis in comparison with 3T proton magnetic resonance spectroscopy. *Eur J Gastroenterol Hepatol* 2014;26(1):88–94.
26. Chauhan A, Sultan LR, Furth EE, Jones LP, Khungar V, Sehgal CM. Diagnostic accuracy of hepatorenal index in the detection and grading of hepatic steatosis. *J Clin Ultrasound* 2016;44(9):580–586.
27. Moret A, Boursier J, Houssel Debry P, et al. Evaluation of the Hepatorenal B-Mode Ratio and the “Controlled Attenuation Parameter” for the Detection and Grading of Steatosis. *Ultraschall Med* 2020.
28. Petzold G, Lasser J, Rühl J, et al. Diagnostic accuracy of B-Mode ultrasound and Hepatorenal Index for graduation of hepatic steatosis in patients with chronic liver disease. *PLoS One* 2020;15(5):e0231044.
29. Tanpowpong N, Panichyawat S. Comparison of sonographic hepatorenal ratio and the degree of hepatic steatosis in magnetic resonance imaging-proton density fat fraction. *J Ultrasound* 2020;20(82):e169–e175.
30. Johnson SI, Fort D, Shortt KJ, et al. Ultrasound Stratification of Hepatic Steatosis Using Hepatorenal Index. *Diagnostics (Basel)* 2021;11(8):1443.
31. Tian BV, Ujita K, Taketomi-Takahashi A, Hirasawa H, Suto T, Tsushima Y. Reliability of ultrasound hepatorenal index and magnetic resonance imaging proton density fat fraction techniques in the diagnosis of hepatic steatosis, with magnetic resonance spectroscopy as the reference standard. *PLoS One* 2021;16(8):e0255768.
32. Kjaergaard M, Lindvig KP, Hansen CD, Detlefsen S, Krag A, Thiele M. Hepatorenal Index by B-Mode Ratio Versus Imaging and Fatty Liver Index to Diagnose Steatosis in Alcohol-Related and Nonalcoholic Fatty Liver Disease. *J Ultrasound Med* 2022. 10.1002/jum.15991. Published online April 27, 2022.
33. Pirmoazen AM, Khurana A, Loening AM, et al. Diagnostic Performance of 9 Quantitative Ultrasound Parameters for Detection and Classification of Hepatic Steatosis in Nonalcoholic Fatty Liver Disease. *Invest Radiol* 2022;57(1):23–32.
34. Fetzer D, Rosado-Mendez IM, Wang M, et al. Pulse-Echo Quantitative US Biomarkers for Liver Steatosis: Towards Technical Standardization. *Radiology* (in press).
35. Stahlschmidt FL, Tafarel JR, Menini-Stahlschmidt CM, Baena CP. Hepatorenal index for grading liver steatosis with concomitant fibrosis. *PLoS One* 2021;16(2):e0246837.
36. Rubin JM, Carson PL, Meyer CR. Anisotropic ultrasonic backscatter from the renal cortex. *Ultrasound Med Biol* 1988;14(6):507–511.
37. Insana MF, Hall TJ, Fishback JL. Identifying acoustic scattering sources in normal renal parenchyma from the anisotropy in acoustic properties. *Ultrasound Med Biol* 1991;17(6):613–626.
38. Ito K, Yoshida K, Maruyama H, Mamou J, Yamaguchi T. Acoustic Impedance Analysis with High-Frequency Ultrasound for Identification of Fatty Acid Species in the Liver. *Ultrasound Med Biol* 2017;43(3):700–711.
39. Burckhardt CB. Speckle in ultrasound B-mode scans. *IEEE Trans Sonics Ultrason* 1978;25(1):1–6.
40. Wagner RF, Smith SW, Sandrik JM, Lopez H. Statistics of Speckle in Ultrasound B-Scans. *IEEE Trans Sonics Ultrason* 1983;30(3):156–163.
41. Wear KA, Wagner RF, Brown DG, Insana MF. Statistical properties of estimates of signal-to-noise ratio and number of scatterers per resolution cell. *J Acoust Soc Am* 1997;102(1):635–641.
42. Lizzi FL, Greenebaum M, Feleppa EJ, Elbaum M, Coleman DJ. Theoretical framework for spectrum analysis in ultrasonic tissue characterization. *J Acoust Soc Am* 1983;73(4):1366–1373.
43. Sehgal CM, Greenleaf JF. Scattering of ultrasound by tissues. *Ultrason Imaging* 1984;6(1):60–80.
44. Madsen EL, Insana MF, Zagzebski JA. Method of data reduction for accurate determination of acoustic backscatter coefficients. *J Acoust Soc Am* 1984;76(3):913–923.
45. Waag RC. A review of tissue characterization from ultrasonic scattering. *IEEE Trans Biomed Eng* 1984;31(12):884–893.
46. Insana MF, Madsen EL, Hall TJ, Zagzebski JA. Tests of the accuracy of a data reduction method for determination of acoustic backscatter coefficients. *J Acoust Soc Am* 1986;79(5):1230–1236.
47. Wear KA, Milunski MR, Wickline SA, Perez JE, Sobel BE, Miller JG. Differentiation between acutely ischemic myocardium and zones of completed infarction in dogs on the basis of frequency-dependent backscatter. *J Acoust Soc Am* 1989;85(6):2634–2641.
48. Insana MF, Wagner RF, Brown DG, Hall TJ. Describing small-scale structure in random media using pulse-echo ultrasound. *J Acoust Soc Am* 1990;87(1):179–192.
49. Chen X, Phillips D, Schwarz KQ, Mottley JG, Parker KJ. The measurement of backscatter coefficient from a broadband pulse-echo system: a new formulation. *IEEE Trans Ultrason Ferroelectr Freq Control* 1997;44(2):515–525.
50. Lavarello RJ, Ghoshal G, Oelze ML. On the estimation of backscatter coefficients using single-element focused transducers. *J Acoust Soc Am* 2011;129(5):2903–2911.
51. Lavarello R, Oelze M. Quantitative ultrasound estimates from populations of scatterers with continuous size distributions. *IEEE Trans Ultrason Ferroelectr Freq Control* 2011;58(4):744–753.

52. Lavarello R, Oelze M. Quantitative ultrasound estimates from populations of scatterers with continuous size distributions: effects of the size estimator algorithm. *IEEE Trans Ultrason Ferroelectr Freq Control* 2012;59(9):2066–2076.
53. Han A, Abuhabsah R, Miller RJ, Sarwate S, O'Brien WD Jr. The measurement of ultrasound backscattering from cell pellet biophantoms and tumors ex vivo. *J Acoust Soc Am* 2013;134(1):686–693.
54. Han A, O'Brien W Jr. Structure function for high-concentration biophantoms of polydisperse scatterer sizes. *IEEE Trans Ultrason Ferroelectr Freq Control* 2015;62(2):303–318.
55. Oelze ML, Mamou J. Review of Quantitative Ultrasound: Envelope Statistics and Backscatter Coefficient Imaging and Contributions to Diagnostic Ultrasound. *IEEE Trans Ultrason Ferroelectr Freq Control* 2016;63(2):336–351.
56. Cloutier G, Destrempes F, Yu F, Tang A. Quantitative ultrasound imaging of soft biological tissues: a primer for radiologists and medical physicists. *Insights Imaging* 2021;12(1):127.
57. Destrempes F, Cloutier G. A critical review and uniformized representation of statistical distributions modeling the ultrasound echo envelope. *Ultrasound Med Biol* 2010;36(7):1037–1051.
58. Baek J, Poul SS, Swanson TA, Tuthill T, Parker KJ. Scattering Signatures of Normal versus Abnormal Livers with Support Vector Machine Classification. *Ultrasound Med Biol* 2020;46(12):3379–3392.
59. Destrempes F, Cloutier G. Statistical modeling of ultrasound signals related to the packing factor of wave scattering phenomena for structural characterization. *J Acoust Soc Am* 2021;150(5):3544–3556.
60. Tuthill TA, Sperry RH, Parker KJ. Deviations from Rayleigh statistics in ultrasound speckle. *Ultrasound Imaging* 1988;10(2):81–89.
61. Bae JS, Lee JY, Lee DH, Kim H, Lee Y, Han JK. Quantitative Evaluation of Hepatic Steatosis Using Normalized Local Variance in a Rat Model: Comparison with Histopathology as the Reference Standard. *Korean J Radiol* 2019;20(9):1399–1407.
62. Bae JS, Lee DH, Lee JY, et al. Quantitative Assessment of Fatty Liver using Ultrasound with Normalized Local Variance Technique. *Ultraschall Med* 2021;42(6):599–606.
63. Jeon SK, Joo I, Kim SY, et al. Quantitative ultrasound radiofrequency data analysis for the assessment of hepatic steatosis using the controlled attenuation parameter as a reference standard. *Ultrasonography* 2021;40(1):136–146.
64. Park J, Lee JM, Lee G, Jeon SK, Joo I. Quantitative Evaluation of Hepatic Steatosis Using Advanced Imaging Techniques: Focusing on New Quantitative Ultrasound Techniques. *Korean J Radiol* 2022;23(1):13–29.
65. Yao LX, Zagzebski JA, Madsen EL. Backscatter coefficient measurements using a reference phantom to extract depth-dependent instrumentation factors. *Ultrasound Imaging* 1990;12(1):58–70.
66. Labyed Y, Milkowski A. Novel Method for Ultrasound-Derived Fat Fraction Using an Integrated Phantom. *J Ultrasound Med* 2020;39(12):2427–2438.
67. Bamber JC, Hill CR, King JA. Acoustic properties of normal and cancerous human liver-II. Dependence of tissue structure. *Ultrasound Med Biol* 1981;7(2):135–144.
68. Nicholas D. Evaluation of backscattering coefficients for excised human tissues: results, interpretation and associated measurements. *Ultrasound Med Biol* 1982;8(1):17–28.
69. *IEEE Trans Sonics Ultrason* 1985;32(3):450–457.
70. Wear KA, Garra BS, Hall TJ. Measurements of ultrasonic backscatter coefficients in human liver and kidney in vivo. *J Acoust Soc Am* 1995;98(4):1852–1857.
71. Lu ZF, Zagzebski JA, Lee FT. Ultrasound backscatter and attenuation in human liver with diffuse disease. *Ultrasound Med Biol* 1999;25(7):1047–1054.
72. Lin SC, Heba E, Wolfson T, et al. Noninvasive Diagnosis of Nonalcoholic Fatty Liver Disease and Quantification of Liver Fat Using a New Quantitative Ultrasound Technique. *Clin Gastroenterol Hepatol* 2015;13(7):1337–1345.e6.
73. Han A, Zhang YN, Boehringer AS, et al. Assessment of Hepatic Steatosis in Nonalcoholic Fatty Liver Disease by Using Quantitative US. *Radiology* 2020;295(1):106–113.
74. Sullivan DC, Obuchowski NA, Kessler LG, et al. Metrology Standards for Quantitative Imaging Biomarkers. *Radiology* 2015;277(3):813–825.
75. Wear KA. Fundamental precision limitations for measurements of frequency dependence of backscatter: applications in tissue-mimicking phantoms and trabecular bone. *J Acoust Soc Am* 2001;110(6):3275–3282.
76. Madsen EL, Dong F, Frank GR, et al. Interlaboratory comparison of ultrasonic backscatter, attenuation, and speed measurements. *J Ultrasound Med* 1999;18(9):615–631.
77. Wear KA, Stiles TA, Frank GR, et al. Interlaboratory comparison of ultrasonic backscatter coefficient measurements from 2 to 9 MHz. *J Ultrasound Med* 2005;24(9):1235–1250.
78. Anderson JJ, Herd MT, King MR, et al. Interlaboratory comparison of backscatter coefficient estimates for tissue-mimicking phantoms. *Ultrasound Imaging* 2010;32(1):48–64.
79. Nam K, Rosado-Mendez IM, Wirtzfeld LA, et al. Ultrasonic attenuation and backscatter coefficient estimates of rodent-tumor-mimicking structures: comparison of results among clinical scanners. *Ultrasound Imaging* 2011;33(4):233–250.
80. Wirtzfeld LA, Nam K, Labyed Y, et al. Techniques and evaluation from a cross-platform imaging comparison of quantitative ultrasound parameters in an in vivo rodent fibroadenoma model. *IEEE Trans Ultrason Ferroelectr Freq Control* 2013;60(7):1386–1400.
81. Paige JS, Bernstein GS, Heba E, et al. A Pilot Comparative Study of Quantitative Ultrasound, Conventional Ultrasound, and MRI for Predicting Histology-Determined Steatosis Grade in Adult Nonalcoholic Fatty Liver Disease. *AJR Am J Roentgenol* 2017;208(5):W168–W177.
82. Han A, Andre MP, Deiranieh L, et al. Repeatability and Reproducibility of the Ultrasonic Attenuation Coefficient and Backscatter Coefficient Measured in the Right Lobe of the Liver in Adults With Known or Suspected Nonalcoholic Fatty Liver Disease. *J Ultrasound Med* 2018;37(8):1913–1927.
83. Han A, Labyed Y, Sy EZ, et al. Inter-sonographer reproducibility of quantitative ultrasound outcomes and shear wave speed measured in the right lobe of the liver in adults with known or suspected non-alcoholic fatty liver disease. *Eur Radiol* 2018;28(12):4992–5000.
84. Han A, Zhang YN, Boehringer AS, et al. Inter-platform reproducibility of ultrasonic attenuation and backscatter coefficients in assessing NAFLD. *Eur Radiol* 2019;29(9):4699–4708.
85. Parker KJ, Tuthill TA, Baggs RB. The role of glycogen and phosphate in ultrasonic attenuation of liver. *J Acoust Soc Am* 1988;83(1):374–378.
86. Tuthill TA, Baggs RB, Parker KJ. Liver glycogen and water storage: effect on ultrasound attenuation. *Ultrasound Med Biol* 1989;15(7):621–627.
87. Barr RG, Ferraioli G, Palmeri ML, et al. Elastography Assessment of Liver Fibrosis: Society of Radiologists in Ultrasound Consensus Conference Statement. *Radiology* 2015;276(3):845–861.
88. Ferraioli G, Wong VW, Castera L, et al. Liver Ultrasound Elastography: An Update to the World Federation for Ultrasound in Medicine and Biology Guidelines and Recommendations. *Ultrasound Med Biol* 2018;44(12):2419–2440.
89. Samir AE, Dhyani M, Vij A, et al. Shear-wave elastography for the estimation of liver fibrosis in chronic liver disease: determining accuracy and ideal site for measurement. *Radiology* 2015;274(3):888–896.
90. Barr RG, Wilson SR, Rubens D, Garcia-Tsao G, Ferraioli G. Update to the Society of Radiologists in Ultrasound Liver Elastography Consensus Statement. *Radiology* 2020;296(2):263–274.
91. Rouyer J, Torres G, Urban MW, Lavarello R. Tissue characterization using simultaneous estimation of backscatter coefficient and elastic shear modulus. *Annu Int Conf IEEE Eng Med Biol Soc* 2016;2016:2881–2884.
92. Goss SA, Johnston RL, Dunn F. Comprehensive compilation of empirical ultrasonic properties of mammalian tissues. *J Acoust Soc Am* 1978;64(2):423–457.
93. Wagner DR. Ultrasound as a tool to assess body fat. *J Obes* 2013;2013:280713.
94. Nguyen TN, Podkova AS, Tam AY, et al. Characterizing Fatty Liver in vivo in Rabbits, Using Quantitative Ultrasound. *Ultrasound Med Biol* 2019;45(8):2049–2062.
95. Deeba F, Schneider C, Mohammed S, et al. A multiparametric volumetric quantitative ultrasound imaging technique for soft tissue characterization. *Med Image Anal* 2021;74:102245.
96. Timana J, Chahua H, Basavarajappa L, Basarab A, Hoyt K, Lavarello R. Simultaneous Imaging of Ultrasonic Backscatter and Attenuation Coefficients for Liver Steatosis Detection in a Murine Animal Model. In: 2022 IEEE 19th International Symposium on Biomedical Imaging (ISBI), Kolkata, India, March 28–31, 2022. Piscataway, NJ: IEEE, 2022; 1–4.
97. Franceschini E, Yu FT, Cloutier G. Simultaneous estimation of attenuation and structure parameters of aggregated red blood cells from backscatter measurements. *J Acoust Soc Am* 2008;123(4):EL85–EL91.
98. Nam K, Zagzebski JA, Hall TJ. Simultaneous backscatter and attenuation estimation using a least squares method with constraints. *Ultrasound Med Biol* 2011;37(12):2096–2104.
99. Shiralkar K, Johnson S, Bluth EI, Marshall RH, Dornelles A, Gulotta PM. Improved method for calculating hepatic steatosis using the hepatorenal index. *J Ultrasound Med* 2015;34(6):1051–1059.